Unveiling the interplay of electronic and phononic excitations in laser-induced oxygen activation on Ru(0001)

Wang, X.; Wang, J.; Spiering, P.; Liu, L.; Meyer, J.; LaRue, J.L.; Xin, H.

The Journal of Chemical Physics

RESEARCH ARTICLE | SEPTEMBER 17 2025

Unveiling the interplay of electronic and phononic excitations in laser-induced oxygen activation on Ru(0001)

Special Collection: Simulation of excited state dynamics in molecular and condensed-matter systems

Xiangrui Wang ; Jiamin Wang; Paul Spiering ; Liping Liu ; Jörg Meyer ; Jerry L. LaRue ; Hongliang Xin

J. Chem. Phys. 163, 114109 (2025)
https://doi.org/10.1063/5.0278197

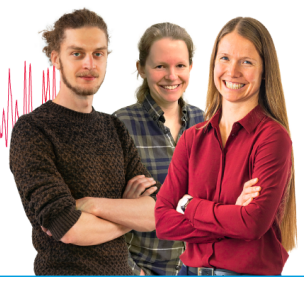

The Journal of Chemical Physics ARTICLE pubs.aip.org/aip/jcp

Unveiling the interplay of electronic and phononic excitations in laser-induced oxygen activation on Ru(0001)

Cite as: J. Chem. Phys. 163, 114109 (2025); doi: 10.1063/5.0278197
Submitted: 28 April 2025 • Accepted: 27 August 2025 •
Published Online: 17 September 2025

Xiangrui Wang,[1] Jiamin Wang,[1] Paul Spiering,[2] Liping Liu,[1] Jörg Meyer,[2,a)] Jerry L. LaRue,[3] and Hongliang Xin[1,a)]

AFFILIATIONS

[1] Department of Chemical Engineering, Virginia Polytechnic Institute and State University, Blacksburg, Virginia 24061, USA
[2] Leiden Institute of Chemistry, Gorlaeus Laboratories, Leiden University, P.O. Box 9502, 2300 RA Leiden, The Netherlands
[3] Schmid College of Science and Technology, Chapman University, Orange, California 92866, USA

Note: This paper is part of the Special Topic, Simulation of excited state dynamics in molecular and condensed-matter systems.
[a)]**Authors to whom correspondence should be addressed:** hxin@vt.edu and j.meyer@chem.leidenuniv.nl

ABSTRACT

Understanding laser-induced dynamics on metal surfaces poses significant challenges due to the intricate interplay between electronic and phononic degrees of freedom, which evolve on distinct timescales. In this study, we introduce a machine learning-accelerated approach to molecular dynamics simulations that incorporates anisotropic electronic friction, providing deeper insights into these complex processes. Our framework extends the accessible time and length scales for nonadiabatic dynamics simulations, enabling a detailed investigation of the laser-induced activation of oxygen on the Ru(0001) surface. Statistical analysis reveals that strong electronic excitation dominates the first 800 fs after laser exposure. Beyond this timescale, energy deposited by electronic excitation continues to drive oxygen activation, while phonons, although always present as a dissipation channel, play a weaker role by buffering energy loss and redistributing kinetic energy among vibrational modes. The observed non-linear yield–fluence relationship, described by $Y \sim F^n$, underscores the pivotal role of electronic excitation. In addition, we identify the z-direction as the key activation mode for oxygen diffusion, with the exponent of the power law representing the quantized energy required for this process. This approach significantly accelerates dynamic simulations while offering valuable insights into the interplay between electronic and phononic excitations during laser-induced oxygen activation on Ru(0001).

I. INTRODUCTION

The dynamics of adsorbates on metal surfaces induced by femtosecond-laser (FL) excitation have broad applications, ranging from materials processing and time-resolved spectroscopy to surface photochemistry.[1,2] Among these, laser-induced surface reactions have garnered significant interest. When an FL pulse excites near-surface electrons in a metal, the low heat capacity of the electron gas leads to a rapid increase in electron temperature. The rapid scattering of these electrons induces thermalization, resulting in a hot Fermi–Dirac distribution. These excited electrons transfer energy to the adsorbates, profoundly influencing surface chemistry,[3–5] for example, by selectively driving bond formation or cleavage and opening new reaction pathways.[6]

The energy transfer between hot electrons and adsorbates occurs through two mechanisms on different timescales, as illustrated in Fig. 1(a): (1) Direct coupling between hot electrons and adsorbates,[7–10] in which electrons populate unoccupied molecular orbitals, occurs within 0.1–1 picoseconds (ps). This process allows the system to transition between different potential energy surfaces (PESs).[11] (2) Alternatively, energy transfer occurs through electron–phonon coupling, where the electron subsystem transfers energy to substrate phonons, which subsequently equilibrate with the adsorbates.[12] This process unfolds over a longer timescale, spanning several picoseconds, as the system remains on the ground-state PES while electrons and phonons gradually reach equilibrium. In this scenario, energy initially deposited in the electronic degrees of freedom is transferred to substrate phonons, with the

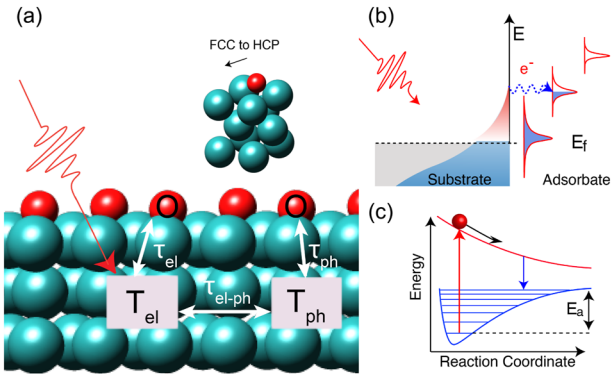

FIG. 1. (a) Schematic representation of energy flow at the Ru surface following FL excitation. The inset illustrates the subsequent motion of the oxygen adsorbate. (b) In the friction-based model, hot electrons excite the system by populating an empty resonance state of the adsorbate. Electron transfer between the metal and the adsorbate induces a dynamic charge redistribution, experienced as electronic friction, which influences the adsorbate's motion. (c) In the DIET model, repeated excitation–deexcitation cycle deposits vibrational energy into the system. In the DIMET model, multiple such cycles further accumulate energy, which can be converted into kinetic energy, allowing the adsorbate to overcome energy barriers and move across the surface.

adsorbates acquiring energy through their equilibration with lattice phonons.[13–16]

The Born–Oppenheimer approximation (BOA) serves as a foundational framework for describing dynamical processes on metal surfaces. Under this approximation, electrons are assumed to rapidly adjust to changes in nuclear positions due to their significantly smaller mass, allowing nuclei to evolve on a ground-state PES.[17–19] Over the past two decades, the necessity of going beyond the BOA has been extensively explored in the context of reactive scattering.[20,21] For systems excited by FL pulses, the BOA breaks down immediately due to the strong coupling between nuclear motion and electronic degrees of freedom.[22] Advances in theoretical and computational methods for describing FL-induced chemical dynamics have thus been deeply informed by progress in reactive scattering.

There are two primary theoretical frameworks for describing the nonadiabatic coupling between adsorbate motions and metal electrons, distinguished by how they account for nonadiabaticity. The first framework, the molecular dynamics with electronic friction (MDEF), models energy transfer through electronic friction and applies in the regime of weak molecule–surface coupling, where the width of the adsorbate resonance state (Δ_a) exceeds the excitation energy ($\varepsilon_a - \varepsilon_F$). In this regime, energy exchange between the substrate and adsorbate can be understood using the Newns–Anderson model,[23] as illustrated in Fig. 1(b). As the adsorbate approaches the substrate, its resonance state shifts downward and broadens. When hot electrons from the substrate populate this broadened state, the adsorbate undergoes charge-induced motion, altering both the energy level and width of the resonance state. The subsequent depopulation of this state generates a dynamic process of filling and emptying, which manifests as electronic friction. This coupling between the electronic bath and nuclear motion governs energy transfer. Excited electrons exert a frictional force on the nuclei, while the de-excitation of electrons induces a random force on the nuclei that depends on the electron temperature.[7,10,24] In the weak-coupling regime, the energy levels involved are typically just above the Fermi level, and nuclear motion can be effectively described by the Langevin equation, which treats the system as residing in its ground state. This approach has been successfully applied to a wide range of systems.[25–34] The second framework is based on the desorption induced by electronic transitions (DIET) theory, which is applicable to systems with strong molecule–surface coupling, where the width of the adsorbate resonance state (Δ_a) is much smaller than the excitation energy ($\varepsilon_a - \varepsilon_F$). In this case, when a hot electron from the substrate excites an empty adsorbate resonance state, a transient negative ion (TNI) is formed.[35,36] This process promotes the system to an excited PES, where relaxation occurs due to the shift in equilibrium position relative to the ground state. As the system returns to the ground state, the nuclei gain vibrational energy. For cases involving high excitation density, the desorption induced by multiple electronic transitions (DIMET) theory applies. Here, the repeated cycles of excitation and de-excitation can occur before the system returns to the ground state, allowing the adsorbate to accumulate vibrational energy. This accumulated energy can eventually enable the adsorbate to overcome the reaction barrier, as illustrated in Fig. 1(c). The experimentally observed nonlinear dependence of reaction yield on absorbed laser fluence provides strong evidence for these repeated excitation/de-excitation cycles.[37,38]

CO oxidation on Ru surfaces is a widely studied example of FL-induced chemistry. Laser excitation has been shown to open a reaction channel for CO oxidation on Ru surfaces that is inaccessible through thermal excitation.[22] Subsequent research has revealed that CO oxidation occurs after atomic oxygen is activated, forming a transition state with a tilted CO on the Ru(0001) surface.[39] Upon laser pulse excitation, photons absorbed by the metallic substrate thermalize energetic electrons within 100 femtoseconds (fs). Strong electron–electron scattering in the metal leads to a non-equilibrium distribution of hot electrons. These excited electrons significantly influence both the electronic structure and surface chemistry by occupying previously empty electronic states or activating surface atoms and molecules. In the case of CO oxidation, oxygen atoms are thought to be activated through the partial filling of anti-bonding orbitals, which weakens the O–Ru bond.[40] Time-resolved soft X-ray spectroscopy has directly observed this activation, revealing an almost instantaneous shift (within 200 fs) in the core-level spectra (XAS, XES) of adsorbed oxygen on Ru following laser excitation.[41] During this process, the oxygen atom moves from the strongly bonded hollow site to the bridge site, a critical step for subsequent CO_2 formation. Only activated oxygen atoms can approach a tilted CO at the top site and form the required transition state. If this transition state does not form, CO tends to desorb from the surface.[30] In addition, the presence of oxygen on the surface modifies the electronic structure of Ru, influencing CO behavior.[42] The complexity of this configuration has made it challenging to fully elucidate the underlying mechanisms. Moreover, the differing timescales of phononic and electronic excitations further complicate the understanding of fast energy transfer processes. A recent study by Žugec *et al.*[29] employs a machine learning-based approach to address this challenge and investigates the CO and CO_2 desorption processes, yielding results that align well with experimental

data.[43] In this work, we focus specifically on the oxygen activation process, which involves fewer degrees of freedom, providing a clearer understanding of how ultrafast lasers influence adsorbate behavior.

In this paper, we employ the MDEF method to simulate the nonadiabatic dynamics of laser-induced O activation on the Ru(0001) surface. To accelerate the MDEF calculations, we integrate machine learning approaches, using trained models to predict both interatomic forces and electronic friction coefficients. Through statistical analysis of these simulations, we uncover the interplay between phononic and electronic excitations and their relative importance in the oxygen activation process.

II. THEORY

A. Nonadiabatic dynamics model

In MDEF, nonadiabaticity is taken into account through Langevin dynamics.[24] The atomic positions of the adsorbates evolve according to the classical Langevin equation,

$$m_i \frac{d^2 r_{i\alpha}}{dt^2} = F_{i\alpha}(\mathbf{r}) - \eta_{i\alpha}(\mathbf{r}_i)\frac{dr_{i\alpha}}{dt} + R_{el,i\alpha}[T_{el}(t), \eta_{i\alpha}(\mathbf{r}_i)], \quad (1)$$

where m_i is the mass of the atom i, $F_{i\alpha}(\mathbf{r}) = -\partial V(\mathbf{r})/\partial r_{i\alpha}$ represents the force acting on the atom i along axis α, derived from the PES. The second term accounts for electronic friction, where $\eta_{i\alpha}(\mathbf{r_i})$ is the diagonal element of the electronic friction tensor and represents the dissipative effect opposing atomic motion along direction α. The last term, $R_{el,i\alpha}$, is a stochastic force with a mean of $\langle R_{el,i\alpha}\rangle = 0$. This stochastic force depends on the electron temperature T_{el} and follows the second fluctuation–dissipation theorem.[44] It is modeled as Gaussian white noise with variance,

$$\mathrm{Var}\left[R_{el,i\alpha}(T_{el}(t), \eta_{i\alpha}(\mathbf{r}_i))\right] = \frac{2k_B T_{el}(t)\eta_{i\alpha}(\mathbf{r}_i)}{\Delta t}, \quad (2)$$

where k_B is the Boltzmann constant, and Δt is the time-integration step. For Ru atoms, a similar Langevin dynamics equation is applied, but the electronic friction coefficient is treated as a constant scalar value. A key advantage of Langevin dynamics lies in its ability to model nonadiabatic energy exchange between nuclear motion and electronic excitations[44] while remaining on the ground-state PES. This approach avoids the explicit inclusion of electronic degrees of freedom, significantly reducing computational cost compared to *ab initio* Ehrenfest dynamics.[45] The electronic friction coefficient accounts for the energy transfer between the substrate and the adsorbate during nuclear motion.[2] Both the friction and random force terms in Langevin dynamics depend on this coefficient. The friction term accounts for the resistance experienced by atoms due to electron excitation, while the random force term captures the energy imparted to atoms as hot electrons relax, thereby accelerating their motion.

One commonly used approach for calculating electronic friction is the local density friction approximation (LDFA),[46] which employs electronic friction coefficients derived from the atom-in-jellium model.[47] While LDFA often yields results that align well with experiments,[48–50] its assumption of isotropy introduces limitations. In reality, energy dissipation is direction-dependent, meaning the frictional force should vary based on the adsorbate's motion. The lack of anisotropy in LDFA has raised concerns about its accuracy for certain systems.[51–53] To address this limitation, electronic friction based on the time-dependent perturbation theory (TDPT)[49,54,55] has been employed. This method explicitly considers the electronic states of the molecule–surface system and provides anisotropic friction coefficients, making it commonly referred to as orbital-dependent friction (ODF). The tensorial nature of electronic friction plays a crucial role in the dissipation process at metal surfaces.[33,56] For instance, as an atom moves in different directions, the rate of energy transfer due to electron–hole pair (EHP) excitations can vary. In cases where the anisotropic nature of electronic friction forces is critical, such as in adatom diffusion, the directional dependence captured by ODF can significantly influence simulation results.

For the diffusion of an oxygen atom on Ru(0001) from the hcp to fcc site along the *y*-axis, we applied both the LDFA and ODF methods to compute the electronic friction coefficient, as shown in Fig. 2. The LDFA method, which provides a scalar and isotropic friction coefficient, exhibits a slight decrease in friction along the minimum energy path, reaching a minimum at the bridge site before increasing again, as illustrated in gray. In contrast, the ODF method, which computes a friction tensor, reveals a pronounced directional dependence. Since the oxygen atom diffuses in the *yz* plane, the *xx* component of the friction tensor does not contribute to energy dissipation along this path. The *yy* component increases and reaches a maximum at the bridge site, while the *zz* component shows minor fluctuations. Notably, both the *yy* and *zz* components are higher at the fcc site than at the hcp site. The diagonal components of the friction tensor are significantly larger—by a factor of 4–7 compared to the isotropic friction coefficient obtained from LDFA, consistent with values reported in Refs. 48 and 57. In this study, we neglect the off-diagonal elements of the friction tensor, as their values are two orders of magnitude smaller than the diagonal components. Consequently, only the diagonal elements are incorporated into the Langevin dynamics, with the friction term along the α direction for atom i denoted as $\eta_{i\alpha}$.

The absorption of photons by the metal surface generates non-equilibrium electron–hole pairs. These hot electrons rapidly thermalize through electron–electron scattering within ~100 fs, resulting in a Fermi–Dirac distribution characterized

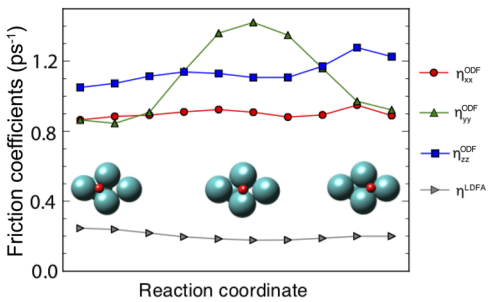

FIG. 2. Electronic friction coefficients for an oxygen atom diffusing from the hcp to fcc site on the Ru(0001) surface along the minimum energy path. The three diagonal components, *xx* (red), *yy* (green), and *zz* (blue), are calculated using the ODF method. The gray line represents the scalar friction coefficient obtained from the LDFA.

by a time-dependent electron temperature $T_{el}(t)$. The subsequent energy transfer from these energetic electrons to the lattice phonons and, ultimately, to the bulk material via heat diffusion can be described by the two-temperature model (2TM).[58] The 2TM characterizes energy dissipation by treating electrons and phonons as two distinct subsystems, each with its own temperature, $T_{el}(t)$ and $T_{ph}(t)$, respectively. These temperatures evolve over time as energy flows between the subsystems through electron–phonon coupling. The model is governed by two coupled differential equations that describe the time evolution of electron and phonon temperatures, with further details provided in the supplementary material.

B. Machine learning interatomic potentials

The machine learning interatomic potentials (MLIPs) have emerged as powerful tools in computational chemistry and materials science, bridging the gap between the accuracy of electronic structure calculations and the efficiency of empirical methods. While approaches such as density functional theory (DFT) provide high accuracy, they are constrained by system size and timescale limitations. In contrast, empirical methods, such as the embedded-atom method (EAM),[59] offer greater computational efficiency but at the expense of accuracy. By leveraging data from electronic structure calculations, MLIPs achieve both high accuracy and computational efficiency, enabling the simulation of large systems over extended timescales.

Early MLIP approaches, such as the artificial neural network (ANN) with symmetry functions developed by Behler and Parrinello,[60] represented the local atomic environment using handcrafted descriptors that were invariant to translation, rotation, and permutation of atoms. While these ANN-based methods demonstrated strong performance across various systems,[61–63] they faced challenges in scaling to multi-element systems and capturing long-range interactions due to their reliance on local descriptors with a fixed cutoff radius. Graph neural networks (GNNs)[64] provide a more flexible alternative by representing chemical structures as graphs, where atoms are nodes and bonds are edges. GNNs employ message-passing schemes that iteratively update node embeddings by aggregating information from neighboring atoms, enabling the capture of long-range interactions. After several message-passing steps, a graph-level embedding is constructed and used to predict properties such as energy and forces. GNN-based MLIPs have been shown to surpass ANN-based methods in accuracy, although at a higher computational cost.[65–67]

In this work, we employ the Atomistic Line Graph Neural Network (ALIGNN)[68] to predict interatomic forces in an O/Ru system for molecular dynamics simulations. Unlike conventional GNN models, ALIGNN incorporates bond angle information by constructing a line graph, where nodes represent the bonds in the original atomistic graph and edges correspond to the angles between bonds. This approach enables the model to capture more intricate atomic interactions, providing a more comprehensive representation of the system's atomic structure. By leveraging both bond distance and angle information, ALIGNN outperforms other GNN models, particularly in systems where angular dependencies play a critical role in determining atomistic properties.

III. SIMULATION DETAILS

A. Friction prediction

The electronic friction coefficient tensor calculated using TDPT is a symmetric matrix.[49] For an oxygen atom on a Ru(0001) fcc site, the friction coefficient tensor is given by

$$\eta^{ODF}(\mathbf{r}_{eq}) = \begin{bmatrix} 0.92 & 0 & 0 \\ 0 & 0.92 & 0 \\ 0 & 0 & 1.28 \end{bmatrix} ps^{-1}. \quad (3)$$

In Langevin dynamics, we consider only the diagonal elements of the friction tensor. For an oxygen atom at its equilibrium position, the assigned friction coefficients are $\eta_{ix} = \eta_{iy} = 0.92$ ps^{-1} and $\eta_{iz} = 1.28$ ps^{-1}, reflecting the anisotropic energy dissipation along different directions, where i denotes the oxygen atom. ODF tensors are calculated using the computational setup described in Refs. 52 and 53. Due to the high computational cost of ODF calculations, a database of ~800 configurations relevant to the MD simulations is constructed. This database is then used to train a machine-learning model. For each atom in these configurations, symmetry functions[60] serve as input features, while the electronic friction coefficient of the oxygen atom is the target value. The dataset is randomly split into 80% for training and 20% for testing. Given the limited dataset size, Gaussian process regression[69] is used for prediction. The electronic friction vector for the adsorbate oxygen atom is predicted using the machine-learning model. The electronic friction coefficient of the Ru atom is taken as 0.35 ps^{-1}, which is computed from the equilibrium geometry of the bulk Ru using ODF and assumed to be constant during dynamic propagation, thereby reducing computational costs. This approximation is commonly employed in MDEF simulation of dynamic processes on metal surfaces and is justified by the fact that the heavy metal atom deviates much less from the equilibrium positions compared to the adsorbate atoms. In Langevin dynamics, for Ru atoms, we assign $\eta_{ix} = \eta_{iy} = \eta_{iz} = 0.35$ ps^{-1}.

B. Machine learning potential construction

Due to the high flexibility of GNNs, their predictions can be unreliable in regions where training data are sparse.[70,71] To efficiently explore the 3N-dimensional space while minimizing redundant DFT calculations, we employ an active learning algorithm based on the query-by-committee[72] method to ensure sufficient sampling coverage. The initial dataset of ~2000 configurations (with $2 \times 2 \times 3$ unit cells) is generated by running *ab initio* Langevin dynamics with a constant friction coefficient (0.002 ps^{-1}) at 2000 K. Multiple GNN models with different hyperparameters are then constructed and initially trained on this dataset. Langevin dynamics is subsequently driven by the GNN model exhibiting the lowest error, with atomic forces predicted on-the-fly to propagate the system. For each newly generated MD configuration, if the model predictions exhibit significant divergence among the different GNN models, indicating a structure not well represented in the existing dataset, DFT calculations are performed to refine the model. Otherwise, the simulation continues to propagate without additional DFT evaluations. The standard deviation of the energies predicted by the multiple GNN models serves as the criterion for determining whether a new image requires a DFT calculation. After sampling

with a 2 × 2 × 3 unit cell, the system is expanded to a larger 4 × 4 × 3 unit cell (at the same oxygen coverage) to mitigate finite-size effects. In each iteration, a batch of newly identified structures is added to the dataset, which is randomly split into a training set (95%) and a testing set (5%). The ALIGNN models are then retrained. Through several iterations, a dataset of 39 721 images is collected, and the best-trained model achieves an accuracy with the RMSE of 3.606 meV/atom.

The DFT calculations are performed using QUANTUM ESPRESSO[73] with the BEEF exchange–correlation functional.[74] The Brillouin zones are sampled with (6 × 6× 1) Monkhorst–Pack *k*-points for the 2 × 2 × 3 unit cell and (3 × 3× 1) for the 4 × 4 × 3 unit cell. The atomic cores are described by ultrasoft pseudopotentials. The occupation of Kohn–Sham eigenstates is smeared using the Fermi–Dirac function with a width of 0.1 eV. There are two oxygen atoms adsorbed on Ru(0001) with 2 × 2 × 3 unit cell supercells and eight oxygen atoms in the 4 × 4 × 3 unit cell (at a 0.5 ML coverage). All unit cells have 17 Å of vacuum space.

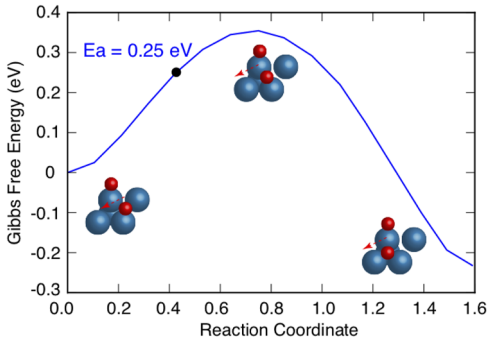

FIG. 3. Gibbs free energy profile of an oxygen atom adsorbed on Ru(0001) as it diffuses from the fcc to the hcp site at 2000 K (phonon temperature). The inflection point is marked with a black dot, with the corresponding Gibbs free energy barrier of E_a = 0.25 eV.

IV. RESULTS AND DISCUSSION

A. Molecular dynamics simulations

MDEF simulations are performed on an O/Ru(0001) system, with a 4 × 4 × 3 unit cell and 8 oxygen atoms adsorbed on the fcc and hcp sites, forming a honeycomb structure (at a coverage of 0.5 ML), on both the movable and the fixed Ru surface. Laser pulses are incorporated using the 2TM, with a pulse width (FWHM) of 50 fs (peaking at t = 0), a wavelength of λ = 400 nm, and four different fluences: 100, 140, 180, and 200 J/m^2. While the phonon temperature is obtained from the 2TM, it is not directly imposed in the Langevin dynamics. Instead, it is determined based on the kinetic energy of the substrate atoms, ensuring a self-consistent description of the system's thermal behavior. A related study employing a similar approach[75] has demonstrated good agreement with theoretical 2TM values over an extended timescale (beyond 14 ps), supporting the validity of this methodology.

Each trajectory starts at the equilibrium structure, following the electron temperature profile obtained from the 2TM. To ensure statistical significance, ~4000 trajectories of molecular dynamics simulations are run for each laser fluence. Each trajectory runs for a total duration of 3000 fs, with a time step of 2 fs. An oxygen atom is considered to be activated if it crosses the inflection point and reaches the high energy region along the DFT-calculated reaction coordinate during diffusion from the hollow site to the bridge site, as shown in Fig. 3. Further details are provided in the supplementary material. In Fig. 3, the position and energy of the initial state are used as reference points. The inset shows the model system (2 × 2 × 3 unit cell) and the reaction path of oxygen from the fcc to the hcp hollow site. The minimal free energy path is obtained using the nudged elastic band (NEB) method with entropic corrections. Because oxygen is strongly bonded to the surface, the entropy correction along the path is minimal at 2000 K (<0.06 eV).

B. Oxygen activation probability and position distribution

The reaction yield (activation probability) progressions are extracted from the molecular dynamics trajectories. The systems propagate from the initial conditions, with the temperature of $T_{el} = T_{ph}$ = 300 K. Due to the significantly lower heat capacity of electrons compared to phonons, the electron temperature rapidly increases, reaching its peak within ~400 fs under all laser fluences. Higher laser fluences result in faster temperature increases and higher peaks, with ~5000 K under F = 100 J/m^2 and over 7000 K under F = 200 J/m^2, as shown in Fig. 4. Subsequently, the energy of these hot electrons is transferred to the phonons through electron–phonon coupling, leading to a gradual rise in the phonon temperature T_{ph}, which reaches its maximum value over a significantly longer timescale. Both T_{el} and T_{ph}, presented in Fig. 4, are obtained from the 2TM. The comparison between the theoretical phonon temperature and the values obtained from the MD simulations is provided in Figs. S7–S10.

From the yield profile in Fig. 4, no oxygen activation is observed during the first 400 fs, as the oxygen atoms do not acquire enough energy to reach the high energy regions. This is further illustrated in the first two plots of Fig. 5, where nearly all oxygen atoms remain confined within the adsorption well, oscillating without approaching the bridge sites. When T_{el} rises sharply at around 400 fs, the fluctuating forces acting on the oxygen atoms become stronger, and the accumulated energy enables them to escape the adsorption wells. Activation begins at this point across all laser fluences, with oxygen atoms approaching the bridge sites. A similar trend has been observed in experiment[41] and simulation.[30] Furthermore, it has been reported that oxygen atoms on fcc sites are more easily activated due to their lower adsorption energy compared to hcp sites.[76] From ~400 to 800 fs, T_{el} decreases from its peak but is still at a high value. The corresponding electronic excitation is strong, and much energy is deposited into the oxygen atoms for them to get activated more easily. This explains the rapid increase in the activation probability during this time, as shown in Fig. 4. By 800 fs, a significant number of oxygen atoms occupy bridge sites, compared to the remaining within the adsorption wells at 400 fs, as depicted in Fig. 5.

After ~800 fs, T_{el} decreases significantly, leading to a noticeable slowdown in the increase in activation probability. This slower growth phase is referred to as the "plateau" period. At this stage, oxygen activation is primarily driven by electronic excitation energy deposited in their translational motion, but electronic excitation

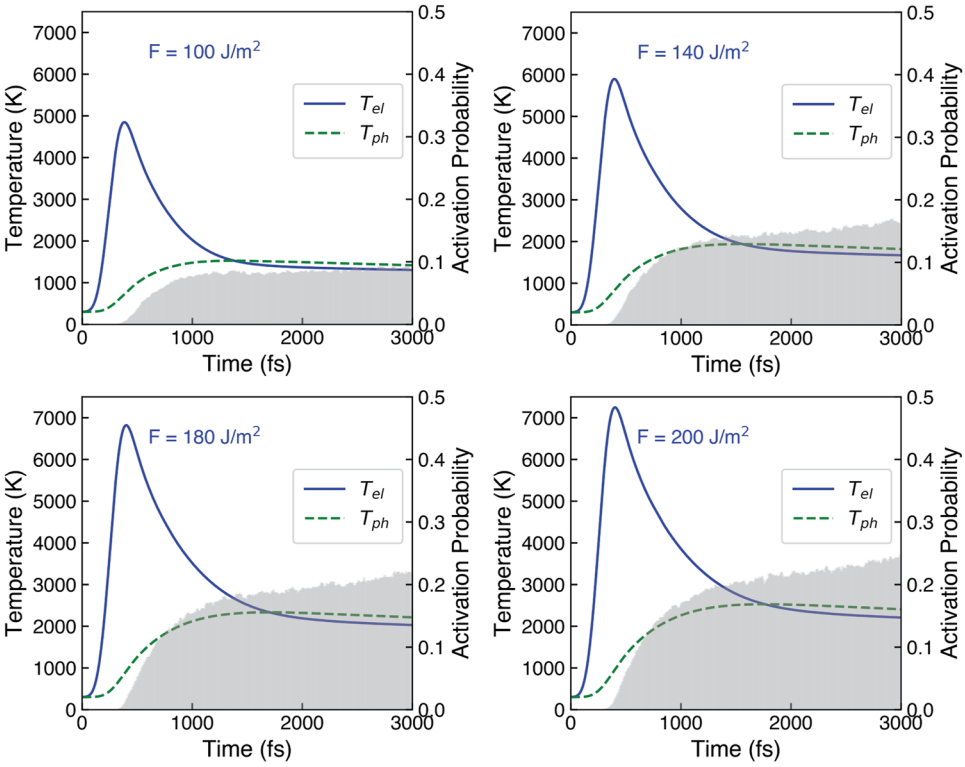

FIG. 4. Time evolution of $T_{el}(t)$ (blue) and $T_{ph}(t)$ (green) for Ru surface models under different laser pulses (F = 100, 140, 180, 200 J/m^2), as predicted by the 2TM. The initial temperature is set to 300 K. The histograms represent the activation probabilities of oxygen on the Ru surface under different laser pulses, showing a rapid increase followed by a plateau. Higher laser fluence leads to a greater activation probability.

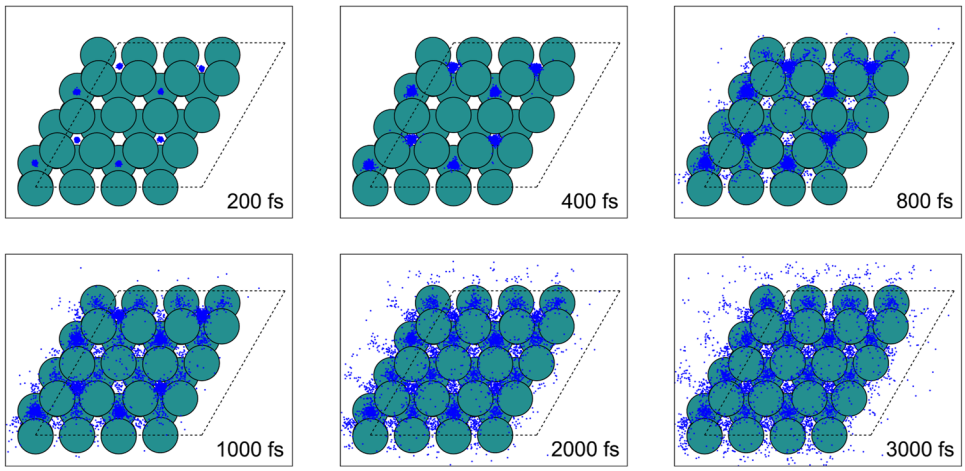

FIG. 5. Distribution of oxygen atom positions in the surface plane (x, y) from MDEF simulations under laser fluence (F = 140 J/m^2), aggregated over all 4000 trajectories. Snapshots are taken at 200, 400, 800, 1000, 2000, and 3000 fs, illustrating the evolution of oxygen diffusion over time.

continues to transfer energy to the adsorbates. Since sufficient energy has already been deposited into the oxygen atoms, they continue to get activated. In this period, the electronic excitation strength decreases but remains significant, with fewer hot electrons available for excitation. The energy already deposited in the nuclear degrees of freedom enhances the mobility and activation probability of oxygen atoms, as illustrated in the last four panels of Fig. 5. While the electronic excitation drives the adsorbates' activation, the energy dissipation process persists throughout the simulation, as excited oxygen atoms continuously transfer energy into the electron bath of the Ru substrate via frictional coupling. This electronic friction leads to kinetic energy loss from the adsorbates. In addition to the ongoing energy loss to electrons, phonon-mediated dissipation becomes increasingly important after 800 fs. At this stage, the thermally excited surface atoms interact dynamically with the oxygen adsorbates. Energy is transferred from the high-energy oxygen atoms to the substrate lattice via nuclear interactions, contributing to phonon excitation, due to the higher temperature of the

adsorbates, shown in Figs. S7–S10. The presence of phonons provides a buffering effect—they do not add energy but moderate its loss by temporarily absorbing and redistributing it. This slows down the decay of kinetic energy in the adsorbates, allowing oxygen atoms to retain energy for activation for a longer time. As a result, the activation probability continues to increase beyond 800 fs, in contrast to the behavior observed on frozen surfaces in Fig. S1. This trend highlights the cooperative role of electronic excitation (as the driver) and phonons (as modulators) in sustaining surface activation over extended timescales. No desorption activity is observed throughout the process, as the diffusion barrier is significantly lower than the desorption energy.[22,77–79] The energy gained from hot surface electrons is insufficient to induce desorption.

When comparing oxygen activation probabilities across different laser fluences, both the rate of increase and the final probability are higher at higher fluences. For instance, the activation probability reaches ~10% at F = 100 J/m^2 and 25% at F = 200 J/m^2, indicating enhanced coupling between substrate electrons and adsorbates and, thus, more deposited energy. Higher laser fluences correspond to higher energy density. The frictional model shows elevated electron temperatures and stronger stochastic forces acting on the oxygen atoms. From the perspective of the DIMET mechanism,[44] higher fluences increase the frequency of excitation–deexcitation cycles[80] before the oxygen atoms relax, which deposits more energy into the system.

C. Kinetic energy and apparent activation barrier

1. Kinetic energy

The time evolution of the mean kinetic energy of the adsorbates is shown in the upper part of Fig. 6, with components separated into the horizontal (xy-plane) and vertical (z-axis) directions. The data reveal a clear correlation between kinetic energy and activation probability: a rapid initial increase before ~800 fs, followed by a plateau. The plateau is observed in both activation probability and kinetic energy and corresponds to the increased mobility of oxygen atoms after 800 fs, as shown in Fig. 5. The rapid increase in kinetic energy at ~400 fs is attributed to high electron temperatures, indicating strong electronic excitation. After that, the rate of kinetic energy increase slows, consistent with the declining electron temperature and weaker electronic excitation. However, despite this reduction, the adsorbate kinetic energy remains elevated, and surface atoms continue to display enhanced mobility, as shown in Fig. 5. This sustained mobility is attributed to the deposited electronic energy.

The concept of energy equipartition among different degrees of freedom is characteristic of systems in thermal equilibrium.[34] A deviation from this equipartition provides evidence for an electron-driven mechanism. As shown in Fig. 6, such a deviation occurs around 400–800 fs, when the high electron temperature causes an abrupt increase in kinetic energy. During this period, a higher proportion of energy is allocated to the z-direction, with its kinetic energy exceeding the x- and y-components. This anisotropic energy distribution reflects the nature of electronic excitation, which predominantly transfers energy into out-of-plane motion due to the orbital orientation and interaction geometry. The system remains in a nonquasithermalized state,[81,82] further supporting the role of electronic excitation as the dominant energy source. As shown in Fig. S3, the deviation from energy equipartition persists until nearly the end of the simulation timescale, especially in the frozen surface case. This shows that the electronic excitation is important throughout the process. In the movable surface system, coupling to phonons promotes gradual thermalization, redistributing the excess kinetic energy from the z-direction into the xy-directions and facilitating more isotropic motion. In contrast, without phonon coupling, as in the frozen surface system, this redistribution is hindered, and the z-axis anisotropy persists. This difference is critical in understanding oxygen activation dynamics. The increase in in-plane (xy-directions) kinetic energy facilitated by phonon-mediated thermalization helps oxygen atoms approach bridge sites more efficiently. Moreover, the motion of the substrate atoms in the movable surface reduces geometric confinement,[28] allowing more favorable configurational transitions. In addition to the kinetic energy redistribution, the lack of phonon buffering and rigid substrate geometry in the frozen surface case cause abrupt energy loss, leading to a rapid drop in kinetic energy and limited activation at later times. Together, these findings underscore a consistent picture: electronic excitation is the primary driver of energy transfer into the adsorbate atoms, while phonons assist by modulating the dissipation rate, redistributing vibrational energy, and reducing confinement, all of which help sustain activation-relevant dynamics over longer timescales.

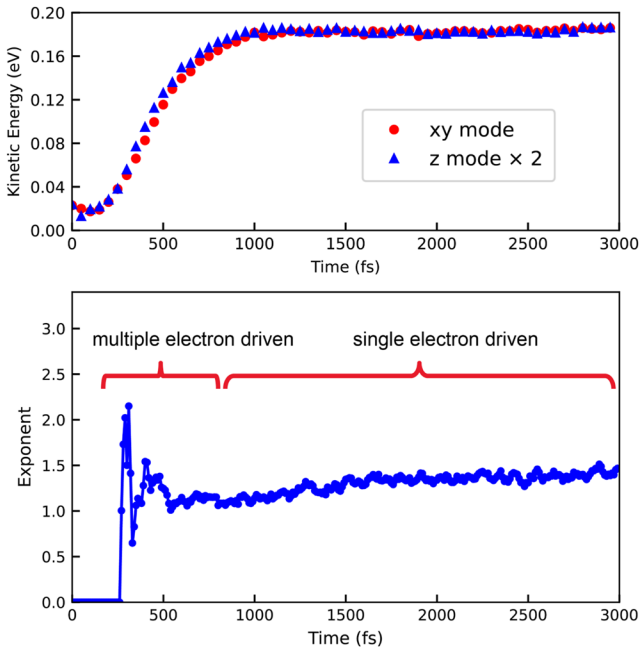

FIG. 6. (Upper) Mean kinetic energy of O atoms on the Ru(0001) surface under a laser fluence of 140 J/m^2. The red circle represents the kinetic energy components in the horizontal plane (xy-plane). The blue triangle represents the kinetic energy component in the vertical direction (z-axis) multiplied by 2. (Lower) Exponent n for laser-induced oxygen atom hopping on the movable Ru surface. The exponent exhibits an abrupt increase at ~300 fs, corresponding to strong electronic excitation, followed by a sharp drop and oscillation. It then stabilizes to around 1 toward the end, indicating a weaker electronic excitation regime.

2. Apparent activation barrier

The reduction of activation barriers under photoinduced conditions has been quantitatively identified in experiments and attributed to electronic excitation effects.[83–85] In this study, we investigate the energy source driving oxygen atom activation by analyzing the reduction in the apparent activation barrier. To achieve this, we determine the apparent activation energy for the oxygen activation probability by fitting the temperature-dependent reaction rates using the Arrhenius equation,[86–88] following an approach commonly used in experiments. Adsorbate temperature is used in this fitting process. It is important to emphasize that the apparent activation barrier here reflects the ensemble averaged activation probability, rather than the intrinsic energy barrier experienced by a single atom on the static potential energy surface. The values of ΔE_a are closely tied to how fast and through what pathways energy is dissipated and should be interpreted as an indicator of the system's non-equilibrium activation dynamics.

The adsorbate temperature is determined using the method outlined in Ref. 32, given by

$$T_{ads} = \frac{2E_{kin}}{3k_B}, \tag{4}$$

where E_{kin} is the mean kinetic energy of all oxygen atoms, averaged over all trajectories obtained from the MDEF simulations. The apparent activation barrier is then extracted by fitting the Arrhenius Law,

$$\ln p = -\frac{\triangle E_a}{k_B}\frac{1}{T_{ads}} + \ln \nu, \tag{5}$$

where $\triangle E_a$ is the apparent activation barrier, p is the activation probability (reaction yield), and ν is the apparent prefactor.

From the apparent activation barrier values in Table I, two key observations can be made: (1) A significant reduction of the activation barrier is observed for the laser-induced nonadiabatic processes (0.404 eV for $F = 100$ J/m^2) compared to the adiabatic thermalized process (0.696 eV). (2) With laser fluence increasing from 100 to 140, the activation barrier further decreases from 0.404 to 0.390 eV. The activation barrier exhibits a laser-dependent behavior.[83] Compared to the thermal activation process in the absence of a laser, the significant decrease in the activation barrier with increasing laser fluence reveals a distinct mechanism driven by electronic excitation. This excitation alters the activation process of oxygen on Ru(0001) by promoting the Ru–O system into an electronically excited state and modifying the energy transfer pathway. Higher laser fluence enhances electronic excitation, facilitating greater energy transfer through the electronic channel. As a result, oxygen atoms become more mobile, leading to a greater likelihood of hopping events.

Interestingly, the apparent activation energy ΔE_a extracted from Arrhenius-type fits is slightly lower on the frozen surface (by ~0.08 eV). The calculated apparent barriers reflect statistical trends rather than single-atom events. Without phonon buffering, energy dissipates more quickly through friction, leading to a short-lived but sharp increase in activation probability with respect to temperature. This steep temperature dependence produces a lower fitted ΔE_a. In contrast, the phonon-assisted dissipation in the movable system spreads activation events over a longer timescale, yielding a smoother temperature dependence and, thus, a higher apparent barrier.

TABLE I. Apparent activation energy for thermal processes and laser-induced processes. An obvious decrease is seen from the adiabatic process to the nonadiabatic processes.

Laser fluence (J/m^2)	$\triangle E_a$ (eV)
0 (DFT)	0.696
100	0.404
140	0.390

D. Non-linear yield–fluence relationship

FL-induced surface reactions typically exhibit a nonlinear relationship between the reaction yield Y (the activation probability in this case) and the absorbed laser fluence F. This relationship follows a power law, given by $Y \sim F^n$, where the fitted exponent typically falls within the range $3 < n < 8$.[37,38,80] However, variations in the electronic structure of the metal and adsorbate, as well as surface morphology effects, can lead to extreme values outside this range.[77] The exponent n has been shown to be indirectly linked to the number of excitation–deexcitation cycles in a DIMET scenario.[81] This framework describes energy transfer between the substrate and the adsorbate in ultrafast laser-induced excitation processes.

In this study, we analyze the temporal evolution of the exponent and qualitatively explain its underlying mechanism using the DIMET framework. At each time step, the exponent is determined by regressing the hopping probabilities against the laser fluences (100, 140, 180, 200 J/m^2), averaged over all the trajectories. The result is shown in the lower part of Fig. 6. Initially, during the 0–300 fs period, the exponent is zero, as no hopping activity is observed. At ~300–400 fs, the exponent abruptly increases, reaching a maximum value of over 2, followed by a sharp drop and oscillation. After 800 fs, it stabilizes to around 1. In this case, the progression of the exponent can be divided into two stages: (1) Before 800 fs, the exponent $n > 1$, indicating that the process is driven by multiple electron excitation–deexcitation cycles. (2) After 800 fs, the exponent $n \approx 1$, suggesting a single electron driven mechanism.

The electron-driven process functions through excitation–deexcitation cycles occurring between the vibrationally excited state PES and the ground-state PES before the system fully relaxes, depositing energy into the vibrational mode. Given the connection between the exponent n and the number of excitation–deexcitation cycles, we analyze these observations within the DIMET framework by examining their respective rates.[80] The deactivation rate is given by

$$k_d = (\tau^{-1} e^{-z/z_d})(1 - f(\varepsilon_A(z), T_{el}(t))), \tag{6}$$

and the activation rate is described in a similar way,

$$k_a = (\tau^{-1} e^{-z/z_d}) f(\varepsilon_A(z), T_{el}(t)), \tag{7}$$

where τ is the excited-state lifetime, z is the distance between the substrate and the adsorbate, and z_d is a range parameter that depends on the vibrational frequency of the O–Ru system. The first term

$(\tau^{-1}e^{-z/z_d})$ represents the hopping rate from the excited PES to the ground-state PES, which is influenced by the relative position of the adsorbate and the substrate. The second term, $f(\varepsilon_A(z), T_e(t))$, is the Fermi factor, which dictates the statistical probability of reaching the electronic final state at a given electron temperature. A higher Fermi factor corresponds to a higher electron temperature, leading to a lower deactivation rate and a higher activation rate, making it easier for the electron to reach the excited state.

When the electron temperature T_e rises sharply at the initial stage and peaks at ~400 fs, the activation rate increases rapidly, while the deactivation rate decreases quickly. These changes enhance the excitations of the Ru–O system, prolonging its residence in the excited state. As a result, the system gains more energy due to a deeper excursion into the excited-state PES, leading to greater energy deposition when it returns to the ground state. In addition to electron temperature, the interaction between the adsorbates and the substrate plays a crucial role. Initially, oxygen atoms remain confined within the adsorption well, oscillating with strong interactions with Ru atoms. This strong coupling is reflected in the rapid increase in the exponent at around 400 fs. Much energy is deposited through the strong electronic expectation, which leads to an increasing activation probability. As the activation probability increases, more oxygen atoms approach bridge sites, where their coordination with Ru atoms is reduced. This decreased interaction, along with the decreased electron temperature, weakens the coupling between hot electrons and the O–Ru system, resulting in a decline in excitation–deexcitation cycles.

As the electron temperature drops greatly after 800 fs, the activation rate decreases and the deactivation rate increases. The electronic excitation becomes weaker, and the exponent n approaches 1. Since the oxygen atoms are already in a vibrationally excited state, a single electron excitation cycle is sufficient for them to overcome the barrier. From the definition of k_a and k_d, they also depend on $\varepsilon_A(z)$, the PES separation, which is defined as $\varepsilon_A(z) = V_e(z) - V_g(z)$. As more oxygen atoms approach bridge sites on the Ru(0001) surface, the separation between the ground-state PES and the transition state decreases. This reduction in $\varepsilon_A(z)$ enhances the electronic excitation at a much slower rate. A slightly stronger excitation is needed because of the consumption of deposited energy, which corresponds to the gradual rise of the exponent value.

In addition to the qualitative analysis, there are quantitative findings that further support our interpretation. At the inflection point, the vibrational energy of oxygen in the z-direction is calculated as $E_{vib} = 0.11$ eV, and the activation barrier is $E_a = 0.25$ eV (see Fig. 3). The ratio m between these two values is given by

$$m = \frac{E_a}{E_{vib}} = \frac{0.25}{0.11} = 2.27. \tag{8}$$

The ratio m indicates that multiple quanta of vibrational energy are required for the oxygen atom to get activated. Notably, the value of m closely aligns with the peak exponent n observed in the statistical analysis, suggesting a direct connection between these quantities. We propose that this correspondence reflects the multiple excitation–deexcitation cycles characteristic of the DIMET regime. Furthermore, this correlation highlights that the z-direction vibrational mode is the dominant mode governing oxygen activation.

In contrast, during the single electron driven process, the exponent $n \approx 1$ suggests that a single quantum of energy is sufficient to overcome the activation barrier. Unlike the earlier time, when multiple excitation–deexcitation cycles were necessary to transfer energy into the vibrational mode, the system at later times has accumulated sufficient kinetic energy. Throughout this process, energy for oxygen diffusion is always supplied by electronic excitations, with the only difference being the number of repeated excitation cycles.

V. SUMMARY AND CONCLUSIONS

In this study, a machine learning-based approach is applied to investigate the femtosecond laser-induced dynamics of oxygen atoms on the Ru(0001) surface, providing insights into the excitation mechanisms governed by electronic and phononic interactions. The key findings are as follows:

(1) Oxygen activation: The activation probability of oxygen atoms initially increases rapidly, followed by a gradual plateau. Under laser excitation, oxygen atoms are activated and migrate from hollow sites to bridge sites. During the first 400 fs, the adsorbates remain within their adsorption wells, after which they begin to get activated. Between 400 and 800 fs, the activation probability surges, with higher laser fluence increasing both the activation rate and overall yield. During this period, electronic excitation dominates, driven by the high electronic temperature.

(2) Kinetic energy trends: The kinetic energy trend of oxygen atoms closely follows the activation probability. The deviation from energy equipartition peaks between 400 and 600 fs and persists until ~3000 fs. This deviation, along with the reduced apparent activation barrier, confirms the dominant role of electronic excitations. The gradual phonon-mediated dissipation buffers the energy loss from the adsorbates and redistributes the excess kinetic energy from the z-direction into in-plane directions, while the flexible surface geometry reduces confinement and facilitates their activation.

(3) Y–F power law and the exponent progression: The Y–F power law exponent progression indicates that electronic excitation dominates in the first 800 fs, after which it weakens. The sharp rise and initial fall of the exponent correlate with electronic temperature, suggesting a mechanism driven by multiple electronic excitations. Once the exponent stabilizes around 1, the system transitions to a single-electron driven mechanism. The exponent also correlates with the number of vibrational quanta required for oxygen activation, highlighting the importance of the z-axis mode. The observed exponent behavior is explained by connecting the results from the friction model to the DIMET framework.

In summary, the activation mechanism of oxygen atoms on Ru(0001) under FL excitation is elucidated through a statistical analysis of ~4000 machine learning molecular dynamics trajectories. The findings confirm that oxygen hopping under ultrafast laser excitations is primarily electron-driven, which is particularly strong within the first 800 fs, after which it decreases. Beyond 800 fs, the electronic excitation gets weaker but still deposits energy into the adsorbates. The deposited energy drives the oxygen activation. The gradual phonon-mediated dissipation buffers the energy loss from

the adsorbates and helps redistribute the kinetic energy. The mobility of Ru atoms reduces the geometric confinement. The selective bond activation facilitated by hot surface electrons presents a potential strategy to overcome scaling constraints and surpass the Sabatier volcano, especially when surface phonon interactions are considered. These insights offer valuable guidance for designing more efficient heterogeneous catalysts and advancing the fundamental understanding of catalytic processes.

SUPPLEMENTARY MATERIAL

The supplementary material provides detailed derivations of the electronic friction tensor and comparisons of reaction probabilities and kinetic energy between relaxed and frozen surfaces. In addition, it outlines the workflow for machine learning-accelerated molecular dynamics simulations and evaluates the performance of the models used in the study.

ACKNOWLEDGMENTS

The project is funded by the NSF CBET Catalysis and the Computational and Data-Enabled Science and Engineering (CDS & E) program (No. CBET-2245402/2245403). The computational resource used in this work is provided by the Advanced Research Computing at Virginia Polytechnic Institute and State University.

AUTHOR DECLARATIONS

Conflict of Interest

The authors have no conflicts to disclose.

Author Contributions

Xiangrui Wang: Data curation (equal); Formal analysis (equal); Investigation (equal); Methodology (equal); Visualization (equal); Writing – original draft (equal); Writing – review & editing (equal). **Jiamin Wang**: Data curation (equal); Formal analysis (equal); Investigation (equal); Methodology (equal); Validation (equal); Writing – original draft (equal). **Paul Spiering**: Data curation (supporting). **Liping Liu**: Methodology (supporting). **Jörg Meyer**: Writing – review & editing (supporting). **Jerry L. LaRue**: Conceptualization (supporting); Funding acquisition (supporting); Supervision (supporting). **Hongliang Xin**: Conceptualization (equal); Funding acquisition (equal); Supervision (equal).

DATA AVAILABILITY

The data that support the findings of this study are available within the article and its supplementary material.

REFERENCES

[1] P. Saalfrank, "Quantum dynamical approach to ultrafast molecular desorption from surfaces," Chem. Rev. **106**, 4116–4159 (2006).
[2] C. Frischkorn and M. Wolf, "Femtochemistry at metal surfaces: Nonadiabatic reaction dynamics," Chem. Rev. **106**, 4207–4233 (2006).
[3] E. D. Potter, J. L. Herek, S. Pedersen, Q. Liu, and A. H. Zewail, "Femtosecond laser control of a chemical reaction," Nature **355**, 66–68 (1992).
[4] J. Y. Park, S. M. Kim, H. Lee, and I. I. Nedrygailov, "Hot-electron-mediated surface chemistry: Toward electronic control of catalytic activity," Acc. Chem. Res. **48**, 2475–2483 (2015).
[5] S. Monturet and P. Saalfrank, "Role of electronic friction during the scattering of vibrationally excited nitric oxide molecules from Au(111)," Phys. Rev. B **82**, 075404 (2010).
[6] S. Funk, M. Bonn, D. N. Denzler, C. Hess, M. Wolf, and G. Ertl, "Desorption of CO from Ru(001) induced by near-infrared femtosecond laser pulses," J. Chem. Phys. **112**, 9888–9897 (2000).
[7] A. C. Luntz, M. Persson, S. Wagner, C. Frischkorn, and M. Wolf, "Femtosecond laser induced associative desorption of H_2 from Ru(0001): Comparison of 'first principles' theory with experiment," J. Chem. Phys. **124**, 244702 (2006).
[8] N. Shenvi, S. Roy, and J. C. Tully, "Dynamical steering and electronic excitation in NO scattering from a gold surface," Science **326**, 829–832 (2009).
[9] B. N. J. Persson and R. Ryberg, "Vibrational damping of adsorbed molecules: Methoxide on Cu(100)," Phys. Rev. Lett. **48**, 549–552 (1982).
[10] A. C. Luntz and M. Persson, "How adiabatic is activated adsorption/associative desorption?," J. Chem. Phys. **123**, 074704 (2005).
[11] M. Baer, "Introduction to the theory of electronic non-adiabatic coupling terms in molecular systems," Phys. Rep. **358**, 75–142 (2002).
[12] A. Douhal and J. Santamaria, Femtochemistry and femtobiology: Ultrafast dynamics in molecular science: University of Castilla-La-Mancha, Toledo, Spain, September 2–6, 2001 (2002).
[13] P. B. Allen, "Theory of thermal relaxation of electrons in metals," Phys. Rev. Lett. **59**, 1460–1463 (1987).
[14] J. Gladh, T. Hansson, and H. Öström, "Electron- and phonon-coupling in femtosecond laser-induced desorption of CO from Ru(0001)," Surf. Sci. **615**, 65–71 (2013).
[15] R. H. M. Groeneveld, R. Sprik, and A. Lagendijk, "Effect of a nonthermal electron distribution on the electron-phonon energy relaxation process in noble metals," Phys. Rev. B **45**, 5079–5082 (1992).
[16] T. Juhasz, H. E. Elsayed-Ali, G. O. Smith, C. Suárez, and W. E. Bron, "Direct measurements of the transport of nonequilibrium electrons in gold films with different crystal structures," Phys. Rev. B **48**, 15488–15491 (1993).
[17] M. Born and R. Oppenheimer, "Zur Quantentheorie der Molekeln," Ann. Phys. **389**, 457–484 (1927).
[18] M. G. Evans and M. Polanyi, "Some applications of the transition state method to the calculation of reaction velocities, especially in solution," Trans. Faraday Soc. **31**, 875–894 (1935).
[19] H. Eyring, H. Gershinowitz, and C. E. Sun, "The absolute rate of homogeneous atomic reactions," J. Chem. Phys. **3**, 786–796 (1935).
[20] M. Alducin, R. Díez Muiño, and J. I. Juaristi, "Non-adiabatic effects in elementary reaction processes at metal surfaces," Prog. Surf. Sci. **92**, 317–340 (2017).
[21] G. J. Kroes and J. Meyer, "Best-of-both-worlds computational approaches to difficult-to-model dissociation reactions on metal surfaces," unpublished, 2024.
[22] M. Bonn, S. Funk, C. Hess, D. N. Denzler, C. Stampfl, M. Scheffler, M. Wolf, and G. Ertl, "Phonon- versus electron-mediated desorption and oxidation of CO on Ru(0001)," Science **285**, 1042–1045 (1999).
[23] D. M. Newns, "Self-consistent model of hydrogen chemisorption," Phys. Rev. **178**, 1123–1135 (1969).
[24] M. Head-Gordon and J. C. Tully, "Molecular dynamics with electronic frictions," J. Chem. Phys. **103**, 10137–10145 (1995).
[25] C. Springer, M. Head-Gordon, and J. C. Tully, "Simulations of femtosecond laser-induced desorption of CO from Cu(100)," Surf. Sci. **320**, L57–L62 (1994).
[26] G. Füchsel, T. Klamroth, S. Monturet, and P. Saalfrank, "Dissipative dynamics within the electronic friction approach: The femtosecond laser desorption of H_2/D_2 from Ru(0001)," Phys. Chem. Chem. Phys. **13**, 8659–8670 (2011).
[27] R. Scholz, S. Lindner, I. Lončarić, J. C. Tremblay, J. I. Juaristi, M. Alducin, and P. Saalfrank, "Vibrational response and motion of carbon monoxide on Cu(100) driven by femtosecond laser pulses: Molecular dynamics with electronic friction," Phys. Rev. B **100**, 245431 (2019).

[28]M. Alducin, N. Camillone, S.-Y. Hong, and J. I. Juaristi, "Electrons and phonons cooperate in the laser-induced desorption of CO from Pd(111)," Phys. Rev. Lett. **123**, 246802 (2019).
[29]I. Žugec, A. Tetenoire, A. S. Muzas, Y. Zhang, B. Jiang, M. Alducin, and J. I. Juaristi, "Understanding the photoinduced desorption and oxidation of CO on Ru(0001) using a neural network potential energy surface," JACS Au **4**, 1997–2004 (2024).
[30]A. Tetenoire, C. Ehlert, J. I. Juaristi, P. Saalfrank, and M. Alducin, "Why ultrafast photoinduced CO desorption dominates over oxidation on Ru(0001)," J. Phys. Chem. Lett. **13**, 8516–8521 (2022).
[31]F. J. Gonzalez, A. S. Muzas, J. I. Juaristi, M. Alducin, and H. F. Busnengo, "Femtosecond laser-induced diffusion and desorption of CO adsorbed on a weak electron–phonon coupling surface: Cu(110)," J. Chem. Phys. **162**, 174701 (2025).
[32]R. Scholz, G. Floß, P. Saalfrank, G. Füchsel, I. Lončarić, and J. I. Juaristi, "Femtosecond-laser induced dynamics of CO on Ru(0001): Deep insights from a hot-electron friction model including surface motion," Phys. Rev. B **94**, 165447 (2016).
[33]M. Askerka, R. J. Maurer, V. S. Batista, and J. C. Tully, "Role of tensorial electronic friction in energy transfer at metal surfaces," Phys. Rev. Lett. **116**, 217601 (2016).
[34]A. Tetenoire, J. I. Juaristi, and M. Alducin, "Disentangling the role of electrons and phonons in the photoinduced CO desorption and CO oxidation on (O,CO)-Ru(0001)," Front. Chem. **11**, 1235176 (2023).
[35]J. W. Gadzuk, "Inelastic resonance scattering, tunneling, and desorption," Phys. Rev. B **44**, 13466–13477 (1991).
[36]J. W. Gadzuk, "Hot-electron femtochemistry at surfaces: On the role of multiple electron processes in desorption," Chem. Phys. **251**, 87–97 (2000).
[37]F. Budde, T. F. Heinz, M. M. T. Loy, J. A. Misewich, F. de Rougemont, and H. Zacharias, "Femtosecond time-resolved measurement of desorption," Phys. Rev. Lett. **66**, 3024–3027 (1991).
[38]J. A. Misewich, A. Kalamarides, T. F. Heinz, U. Höfer, and M. M. T. Loy, "Vibrationally assisted electronic desorption: Femtosecond surface chemistry of O_2/Pd(111)," J. Chem. Phys. **100**, 736–739 (1994).
[39]H. Öström, H. Öberg, H. Xin, J. LaRue, M. Beye, M. Dell'Angela, J. Gladh, M. L. Ng, J. A. Sellberg, S. Kaya, G. Mercurio, D. Nordlund, M. Hantschmann, F. Hieke, D. Kühn, W. F. Schlotter, G. L. Dakovski, J. J. Turner, M. P. Minitti, A. Mitra, S. P. Moeller, A. Föhlisch, M. Wolf, W. Wurth, M. Persson, J. K. Nørskov, F. Abild-Pedersen, H. Ogasawara, L. G. M. Pettersson, and A. Nilsson, "Probing the transition state region in catalytic CO oxidation on Ru," Science **347**, 978–982 (2015).
[40]J. L. LaRue, T. Katayama, A. Lindenberg, A. S. Fisher, H. Öström, A. Nilsson, and H. Ogasawara, "THz-pulse-induced selective catalytic CO oxidation on Ru," Phys. Rev. Lett. **115**, 036103 (2015).
[41]M. Beye, H. Öberg, H. Xin, G. L. Dakovski, M. Dell'Angela, A. Föhlisch, J. Gladh, M. Hantschmann, F. Hieke, S. Kaya, D. Kühn, J. LaRue, G. Mercurio, M. P. Minitti, A. Mitra, S. P. Moeller, M. L. Ng, A. Nilsson, D. Nordlund, J. Nørskov, H. Öström, H. Ogasawara, M. Persson, W. F. Schlotter, J. A. Sellberg, M. Wolf, F. Abild-Pedersen, L. G. M. Pettersson, and W. Wurth, "Chemical bond activation observed with an x-ray laser," J. Phys. Chem. Lett. **7**, 3647–3651 (2016).
[42]H. Xin, J. LaRue, H. Öberg, M. Beye, M. Dell'Angela, J. J. Turner, J. Gladh, M. L. Ng, J. A. Sellberg, S. Kaya, G. Mercurio, F. Hieke, D. Nordlund, W. F. Schlotter, G. L. Dakovski, M. P. Minitti, A. Föhlisch, M. Wolf, W. Wurth, H. Ogasawara, J. K. Nørskov, H. Öström, L. G. M. Pettersson, A. Nilsson, and F. Abild-Pedersen, "Strong influence of coadsorbate interaction on CO desorption dynamics on Ru(0001) probed by ultrafast X-Ray spectroscopy and ab initio simulations," Phys. Rev. Lett. **114**, 156101 (2015).
[43]S. Funk, "Ultraschnelle Reaktionsdynamik an Oberflächen: Desorption und oxidation von CO auf Ru(001) induziert durch Femtosekunden-Laserpulse," Ph.D. thesis. dissertation (Freie Universität Berlin, 1999).
[44]M. Brandbyge, P. Hedegård, T. F. Heinz, J. A. Misewich, and D. M. Newns, "Electronically driven adsorbate excitation mechanism in femtosecond-pulse laser desorption," Phys. Rev. B **52**, 6042–6056 (1995).
[45]X. Li, J. C. Tully, H. B. Schlegel, and M. J. Frisch, "*Ab initio* Ehrenfest dynamics," J. Chem. Phys. **123**, 084106 (2005).
[46]J. I. Juaristi, M. Alducin, R. D. Muiño, H. F. Busnengo, and A. Salin, "Role of electron-hole pair excitations in the dissociative adsorption of diatomic molecules on metal surfaces," Phys. Rev. Lett. **100**, 116102 (2008).
[47]N. Gerrits, J. I. Juaristi, and J. Meyer, "Electronic friction coefficients from the atom-in-jellium model for Z=1–92," Phys. Rev. B **102**, 155130 (2020).
[48]S. P. Rittmeyer, J. Meyer, J. I. Juaristi, and K. Reuter, "Electronic Friction-Based vibrational lifetimes of molecular adsorbates: Beyond the Independent-Atom approximation," Phys. Rev. Lett. **115**, 046102 (2015).
[49]R. J. Maurer, M. Askerka, V. S. Batista, and J. C. Tully, "*Ab initio* tensorial electronic friction for molecules on metal surfaces: Nonadiabatic vibrational relaxation," Phys. Rev. B **94**, 115432 (2016).
[50]S. P. Rittmeyer, J. Meyer, and K. Reuter, "Nonadiabatic vibrational damping of molecular adsorbates: Insights into electronic friction and the role of electronic coherence," Phys. Rev. Lett. **119**, 176808 (2017).
[51]Y. Zhang, R. J. Maurer, H. Guo, and B. Jiang, "Hot-electron effects during reactive scattering of H_2 from Ag(111): The interplay between mode-specific electronic friction and the potential energy landscape," Chem. Sci. **10**, 1089–1097 (2019).
[52]P. Spiering and J. Meyer, "Testing electronic friction models: Vibrational de-excitation in scattering of H_2 and D_2 from Cu(111)," J. Phys. Chem. Lett. **9**, 1803–1808 (2018).
[53]P. Spiering, K. Shakouri, J. Behler, G.-J. Kroes, and J. Meyer, "Orbital-dependent electronic friction significantly affects the description of reactive scattering of N_2 from Ru(0001)," J. Phys. Chem. Lett. **10**, 2957–2962 (2019).
[54]M. Forsblom and M. Persson, "Vibrational lifetimes of cyanide and carbon monoxide on noble and transition metal surfaces," J. Chem. Phys. **127**, 154303 (2007).
[55]W. H. Butler, F. J. Pinski, and P. B. Allen, "Phonon linewidths and electron-phonon interaction in Nb," Phys. Rev. B **19**, 3708–3721 (1979).
[56]M. Askerka, R. J. Maurer, V. S. Batista, and J. C. Tully, "Erratum: Role of tensorial electronic friction in energy transfer at metal surfaces [Phys. Rev. Lett. 116, 217601 (2016)]," Phys. Rev. Lett. **119**, 069901 (2017).
[57]A. C. Luntz, I. Makkonen, M. Persson, S. Holloway, D. M. Bird, and M. S. Mizielinski, "Comment on 'Role of electron-hole pair excitations in the dissociative adsorption of diatomic molecules on metal surfaces'," Phys. Rev. Lett. **102**, 109601 (2009); author reply 109602.
[58]S. I. Anisimov and B. Rethfeld, "Theory of ultrashort laser pulse interaction with a metal," Proc. SPIE **3093**, 192–203 (1997).
[59]M. S. Daw and M. I. Baskes, "Embedded-atom method: Derivation and application to impurities, surfaces, and other defects in metals," Phys. Rev. B **29**, 6443–6453 (1984).
[60]J. Behler and M. Parrinello, "Generalized neural-network representation of high-dimensional potential-energy surfaces," Phys. Rev. Lett. **98**, 146401 (2007).
[61]N. Artrith and A. M. Kolpak, "Grand canonical molecular dynamics simulations of Cu–Au nanoalloys in thermal equilibrium using reactive ANN potentials," Comput. Mater. Sci. **110**, 20–28 (2015).
[62]N. Artrith and A. Urban, "An implementation of artificial neural-network potentials for atomistic materials simulations: Performance for TiO_2," Comput. Mater. Sci. **114**, 135–150 (2016).
[63]J. S. Smith, O. Isayev, and A. E. Roitberg, "ANI-1: An extensible neural network potential with DFT accuracy at force field computational cost," Chem. Sci. **8**, 3192–3203 (2017).
[64]F. Scarselli, M. Gori, A. C. Tsoi, M. Hagenbuchner, and G. Monfardini, "The graph neural network model," IEEE Trans. Neural Networks **20**, 61–80 (2009).
[65]K. Schütt, P.-J. Kindermans, H. E. S. Felix, S. Chmiela, A. Tkatchenko, and K. Müller, "SchNet: A continuous-filter convolutional neural network for modeling quantum interactions," Neural Inf. Process. Syst. **30**, 992–1002 (2017).
[66]J. Gasteiger, S. Giri, J. T. Margraf, and S. Günnemann, "Fast and uncertainty-aware directional message passing for non-equilibrium molecules," Machine Learning for Molecules Workshop, NeurIPS (2020).
[67]J. Gasteiger, F. Becker, and S. Günnemann, "Gemnet: Universal directional graph neural networks for molecules," Adv. Neural Inf. Process. Syst. **34**, 6790–6802 (2021).
[68]K. Choudhary and B. DeCost, "Atomistic line graph neural network for improved materials property predictions," npj Comput. Mater. **7**, 185 (2021).

[69]C. E. Rasmussen and C. K. I. Williams, *Gaussian Processes for Machine Learning* (The MIT Press, 2005).
[70]J. Behler, "Atom-centered symmetry functions for constructing high-dimensional neural network potentials," J. Chem. Phys. **134**, 074106 (2011).
[71]A. A. Peterson, R. Christensen, and A. Khorshidi, "Addressing uncertainty in atomistic machine learning," Phys. Chem. Chem. Phys. **19**, 10978–10985 (2017).
[72]N. Artrith and J. Behler, "High-dimensional neural network potentials for metal surfaces: A prototype study for copper," Phys. Rev. B **85**, 045439 (2012).
[73]P. Giannozzi, S. Baroni, N. Bonini, M. Calandra, R. Car, C. Cavazzoni, D. Ceresoli, G. L. Chiarotti, M. Cococcioni, I. Dabo, A. Dal Corso, S. de Gironcoli, S. Fabris, G. Fratesi, R. Gebauer, U. Gerstmann, C. Gougoussis, A. Kokalj, M. Lazzeri, L. Martin-Samos, N. Marzari, F. Mauri, R. Mazzarello, S. Paolini, A. Pasquarello, L. Paulatto, C. Sbraccia, S. Scandolo, G. Sclauzero, A. P. Seitsonen, A. Smogunov, P. Umari, and R. M. Wentzcovitch, "QUANTUM ESPRESSO: A modular and open-source software project for quantum simulations of materials," J. Phys.: Condens. Matter **21**, 395502 (2009).
[74]J. Wellendorff, K. T. Lundgaard, A. Møgelhøj, V. Petzold, D. D. Landis, J. K. Nørskov, T. Bligaard, and K. W. Jacobsen, "Density functionals for surface science: Exchange-correlation model development with Bayesian error estimation," Phys. Rev. B **85**, 235149 (2012).
[75]A. S Muzas, A. Serrano Jiménez, Y. Zhang, B. Jiang, J. I. Juaristi, and M. Alducin, "Multicoverage study of femtosecond laser-induced desorption of CO from pd(111)," J. Phys. Chem. Lett. **15**, 2587–2594 (2024).
[76]A. Tetenoire, J. I. Juaristi, and M. Alducin, "Insights into the coadsorption and reactivity of O and CO on Ru(0001) and their coverage dependence," J. Phys. Chem. C **125**, 12614–12627 (2021).
[77]K. Stépán, M. Dürr, J. Güdde, and U. Höfer, "Laser-induced diffusion of oxygen on a stepped Pt(111) surface," Surf. Sci. **593**, 54–66 (2005).
[78]A. Böttcher and H. Niehus, "Oxygen adsorbed on oxidized Ru(0001)," Phys. Rev. B **60**, 14396 (1999).
[79]T. E. Madey, H. Albert Engelhardt, and D. Menzel, "Adsorption of oxygen and oxidation of CO on the ruthenium (001) surface," Surf. Sci. **48**, 304–328 (1975).
[80]J. A. Misewich, T. F. Heinz, and D. M. Newns, "Desorption induced by multiple electronic transitions," Phys. Rev. Lett. **68**, 3737–3740 (1992).
[81]M. Nest and P. Saalfrank, "Open-system density matrix description of femtosecond laser desorption of electronically and vibrationally relaxing adsorbates: Single- and two-pulse scenarios," J. Chem. Phys. **116**, 7189–7199 (2002).
[82]G. Füchsel, J. C. Tremblay, T. Klamroth, P. Saalfrank, and C. Frischkorn, "Concept of a single temperature for highly nonequilibrium laser-induced hydrogen desorption from a ruthenium surface," Phys. Rev. Lett. **109**, 098303 (2012).
[83]L. Zhou, D. F. Swearer, C. Zhang, H. Robatjazi, H. Zhao, L. Henderson, L. Dong, P. Christopher, E. A. Carter, P. Nordlander, and N. J. Halas, "Quantifying hot carrier and thermal contributions in plasmonic photocatalysis," Science **362**, 69–72 (2018).
[84]X. Zhang, X. Li, D. Zhang, N. Q. Su, W. Yang, H. O. Everitt, and J. Liu, "Product selectivity in plasmonic photocatalysis for carbon dioxide hydrogenation," Nat. Commun. **8**, 14542 (2017).
[85]Q. Xiao, S. Sarina, A. Bo, J. Jia, H. Liu, D. P. Arnold, Y. Huang, H. Wu, and H. Zhu, "Visible light-driven cross-coupling reactions at lower temperatures using a photocatalyst of palladium and gold alloy nanoparticles," ACS Catal. **4**, 1725–1734 (2014).
[86]S. Arrhenius, "Über die dissociationswärme und den einfluss der temperatur auf den dissociationsgrad der elektrolyte," Z. Phys. Chem. **4U**, 96–116 (1889).
[87]S. Arrhenius, "Über die reaktionsgeschwindigkeit bei der inversion von rohrzucker durch säuren," Z. Phys. Chem. **4**, 226–248 (1889).
[88]K. J. Laidler, "The development of the Arrhenius equation," J. Chem. Educ. **61**, 494 (1984).